TWO-DIMENSIONAL ELECTROMAGNETIC SCATTERING OF NON-PLANE INCIDENT WAVES BY PERIODIC STRUCTURES

K. Watanabe

Department of Information and Communication Engineering
Faculty of Information Engineering
Fukuoka Institute of Technology
3-30-1 Wajirohigashi, Higashi-ku, Fukuoka 811-0295, Japan

K. Yasumoto

Department of Computer Science and Communication Engineering
Graduate School of Information Science and Electrical Engineering
Kyushu University
6-10-1 Hakozaki, Higashi-ku, Fukuoka 812-8581, Japan

Abstract—This paper proposes the pseudo-periodic Fourier transform to analyze the electromagnetic scattering from periodic structures with non-plane wave incidence. The pseudo-periodic Fourier transform converts arbitrary field components into pseudo-periodic functions and the conventional grating theories based on the Floquet theorem become applicable. The inverse transform is given by integrating with respect to the transform parameter over a finite interval and the near field analysis requires numerical integration. Some application examples are numerically examined and the results show good convergence.

1. INTRODUCTION

Periodic structures are widely used in microwave, millimeter-wave, and optical wave regions because of various effects; for example, wave reflection, wavelength or polarization selectivity, mode conversion. Therefore, electromagnetic scattering from periodic structures has been extensively studied, and many analytical and numerical approaches have been developed to analyze the scattering problems. When a plane wave is incident on a periodic structure, the scattered waves propagate to discrete directions. Then most of

the approaches are based on the Floquet theorem, which claims that the electromagnetic fields are pseudo-periodic by assuming plane wave incidence [1]. This means that each field components is a product of a periodic function and an exponential phase factor, and allows us to reduce the analysis region to the single periodicity cell. However, for the problems with non-plane wave incidence, the Floquet theorem is no longer applicable. Surely there are a limited number of papers that address the more realistic situation of the Gaussian beam incidence [2, 3]. The beam field is well approximated by a superposition of a finite number of propagating plane waves because the evanescent plane waves are negligible to express the beam fields. Then, the scattered fields for the beam incidence can be calculated by superposing all the scattered fields for each plane wave component.

Recently, Caloz *et al.* [4] and Jandieri *et al.* [5] developed a numerical approach to analyze radiation from a line source in two-dimensional photonic crystals formed by periodic array of circular cylinders. The aim of the present paper is to propose a novel numerical approach for scattering problems of periodic structures with arbitrary incident waves. For this purpose, we propose a novel transform by extending the concept of the line source array introduced in Refs. [4, 5]. We call it pseudo-periodic Fourier transform (PPFT) because it is similar to the periodic Fourier transform (PFT) developed by Nakayama [6] but makes any function pseudo-periodic. PFT, which makes any function periodic, was originally developed to analyze a scattering problem of a plane wave from a finite periodic surface, and also applied to the propagation analyses in waveguide transition problems [7]. The relation between PFT and PPFT is equivalent to that between the periodic and the pseudo-periodic functions. However, we believe that the periodic property of PPFT with respect to the transform parameter is good for thinking the numerical integration required on the inverse transform. Anyway, PPFT converts an incident field to a pseudo-periodic function and, therefore, it is expressed in the Rayleigh expansion (e.g. plane wave expansion). The scattered fields for each plane wave incidence can be calculated by using the conventional approaches based on the Floquet theorem. PPFT uses a transform parameter, which determines each plane wave incidence, and the inverse transform is given by integrating with respect to the transform parameter over a finite interval. Therefore, the scattered fields for arbitrary incident field are obtained by integrating the scattered field for each transform parameter.

Throughout the paper, we deal with only time-harmonic fields, assuming a time dependence in $\exp(-i\,\omega\,t)$, and the electromagnetic fields and the structures under consideration are uniform in the z-

direction. Two fundamental polarizations are expressed by TE and TM, in which the E and the H fields are respectively perpendicular to the (x, y)-plane. Also, the arguments of complex square roots are taken in $(-\pi/2, \pi/2]$. For numerical purposes, all matrices appeared later have to be truncated in practical computation. We denote the truncation order by N, which truncates the generalized Fourier series expansions from the $-N$th to the Nth order for both incident and scattered fields.

2. BASIC IDEA

2.1. Pseudo-Periodic Fourier Transform

Let $f(x)$ be a function and d be a positive real constant. Then PPFT is defined by the relation:

$$\overline{f}(x; \xi) = \sum_{m=-\infty}^{\infty} f(x - m\,d)\, e^{i\,m\,d\,\xi}, \tag{1}$$

which is implicitly assumed to converge and ξ is a transform parameter. The transformed function $\overline{f}(x; \xi)$ has a pseudo-periodic property with the pseudo-period d in terms of x:

$$\overline{f}(x - m\,d; \xi) = \overline{f}(x; \xi)\, e^{-i\,m\,d\,\xi}, \tag{2}$$

for any integer m. The transformed function has also a periodic property with the period $2\,\pi/d$ in terms of the transform parameter ξ:

$$\overline{f}\left(x; \xi - m\,\frac{2\,\pi}{d}\right) = \overline{f}(x; \xi), \tag{3}$$

and the inverse transform is formally derived as

$$f(x) = \frac{d}{2\,\pi} \int_{-\pi/d}^{\pi/d} \overline{f}(x; \xi)\, d\xi. \tag{4}$$

As written above, the transformed function is pseudo-periodic, and it is therefore expressed in the generalized Fourier series expansion [1]:

$$\overline{f}(x; \xi) = \sum_{n=-\infty}^{\infty} \overline{f}_n(\xi)\, e^{i\,\alpha_n(\xi)\,x} \tag{5}$$

with

$$\alpha_n(\xi) = \xi + n\,\frac{2\,\pi}{d}.\tag{6}$$

The coefficient functions $\overline{f}_n(\xi)$ relates to $\overline{f}(x;\xi)$ and $f(x)$ in the following form:

$$\overline{f}_n(\xi) = \frac{1}{d}\int_{-d/2}^{d/2}\overline{f}(x;\xi)\,e^{-i\,\alpha_n(\xi)\,x}\,dx = \frac{1}{d}\int_{-\infty}^{\infty} f(x)\,e^{-i\,\alpha_n(\xi)\,x}\,dx.\tag{7}$$

2.2. Rayleigh Expansion of Arbitrary Field

Let $\psi(x,y)$ be a two-dimensional wave function satisfying the following Helmholtz equation:

$$\left(\frac{\partial^2}{\partial x^2} + \frac{\partial^2}{\partial y^2} + k_s{}^2\right)\psi(x,y) = 0\tag{8}$$

where k_s is a wavenumber and supposed to be real and constant. We apply PPFT defined by Eq. (1) to this equation. The differential operation in Eq. (8) is unchanged by PPFT, and then the equation is formally transformed into the same form:

$$\left(\frac{\partial^2}{\partial x^2} + \frac{\partial^2}{\partial y^2} + k_s{}^2\right)\overline{\psi}(x;\xi,y) = 0.\tag{9}$$

Since the transformed wave function $\overline{\psi}(x;\xi,y)$ is pseudo-periodic in terms of x with the pseudo-period d, it can be expanded in a generalized Fourier series as Eq. (5):

$$\overline{\psi}(x;\xi,y) = \sum_{n=-\infty}^{\infty}\overline{\psi}_n(\xi,y)\,e^{i\,\alpha_n(\xi)\,x}.\tag{10}$$

This expression is substituted into Eq. (9) and the orthogonality of the exponential functions yields

$$\left(\frac{\partial^2}{\partial y^2} + \beta_{s,n}(\xi)^2\right)\overline{\psi}_n(\xi,y) = 0\tag{11}$$

for arbitrary integer n, where

$$\beta_{s,n}(\xi) = \sqrt{k_s{}^2 - \alpha_n(\xi)^2}.\tag{12}$$

The general solution to Eq. (11) can be expressed as

$$\overline{\psi}_n(\xi, y) = \overline{a}_{s,n}^{(+)}(\xi, y) + \overline{a}_{s,n}^{(-)}(\xi, y) \tag{13}$$

with

$$\overline{a}_{s,n}^{(\pm)}(\xi, y) = \overline{a}_{s,n}^{(\pm)}(\xi, y') \, e^{\pm i \, \beta_{s,n}(\xi)(y-y')} \tag{14}$$

where $\overline{a}_{s,n}^{(+)}(\xi, y')$ and $\overline{a}_{s,n}^{(-)}(\xi, y')$ denote the amplitudes at $y = y'$ propagating in the positive and the negative y-direction, respectively. Substituting into Eq. (10), the transformed wave function $\overline{\psi}(x; \xi, y)$ is expressed in the Rayleigh expansion as

$$\overline{\psi}(x; \xi, y) = \sum_{n=-\infty}^{\infty} \left\{ \overline{a}_{s,n}^{(+)}(\xi, y') \, e^{i[\alpha_n(\xi) \, x + \beta_{s,n}(\xi)(y-y')]} \right.$$
$$\left. + \overline{a}_{s,n}^{(-)}(\xi, y') \, e^{i[\alpha_n(\xi) \, x - \beta_{s,n}(\xi)(y-y')]} \right\}. \tag{15}$$

To treat the expansion functions and coefficients systematically, we introduce column matrices and Eq. (15) is then rewritten as

$$\overline{\psi}(x; \xi, y) = \boldsymbol{f}_s^{(+)}(x; \xi, y - y')^t \, \overline{\boldsymbol{a}}_s^{(+)}(\xi, y')$$
$$+ \boldsymbol{f}_s^{(-)}(x; \xi, y - y')^t \, \overline{\boldsymbol{a}}_s^{(-)}(\xi, y') \tag{16}$$

where $\overline{\boldsymbol{a}}_s^{(+)}(\xi, y')$ and $\overline{\boldsymbol{a}}_s^{(-)}(\xi, y')$ denote the column matrices generated by the amplitude of plane waves, and $\boldsymbol{f}_s^{(+)}(x; \xi, y)$ and $\boldsymbol{f}_s^{(-)}(x; \xi, y)$ are the column matrices of the plane waves given as

$$\left(\boldsymbol{f}_s^{(\pm)}(x; \xi, y) \right)_n = e^{i(\alpha_n(\xi) \, x \pm \beta_{s,n}(\xi) \, y)} \tag{17}$$

where $\alpha_n(\xi)$ and $\beta_{s,n}(\xi)$ denote the propagation constants in the x- and the y-directions, respectively.

2.3. Scattering by Periodic Structures

Here, we consider the scattering of waves from periodic structures contained in a half-space. The x-axis is taken along the periodicity direction, and the periodic scatterer is contained in $y \leq 0$. The other half-space $y > 0$ is filled with a medium described by a wavenumber k_s, and the incident field comes from this side. The fields have to satisfy the Helmholtz equation (8) in the region $y > 0$, and the transformed fields are therefore expressed in the Rayleigh expansions given by

Eq. (16). Considering the propagation direction of the plane waves, the incident and the scattered field are given by the second and the first terms, respectively. If the fictitious pseudo-period d is chosen to be identical to the structural period, $\boldsymbol{f}_s^{(+)}(x; \xi, y)$ and $\boldsymbol{f}_s^{(-)}(x; \xi, y)$ give sets of space-harmonic waves generated by an incident plane wave with the x-directional wavenumber of ξ. Let $\psi^{(i)}(x, y)$ be the incident field that illuminates the periodic structure. Then, the amplitudes of the plane waves propagating downward are given from Eq. (7) as

$$\overline{a}_{s,n}^{(-)}(\xi, +0) = \frac{1}{d} \int_{-\infty}^{\infty} \psi^{(i)}(x, +0)\, e^{-i\,\alpha_n(\xi)\,x}\, dx. \tag{18}$$

The relation between the amplitudes is written in the following form:

$$\overline{\boldsymbol{a}}_s^{(+)}(\xi, +0) = \boldsymbol{S}(\xi)\, \overline{\boldsymbol{a}}_s^{(-)}(\xi, +0) \tag{19}$$

and the scattering-matrix $\boldsymbol{S}(\xi)$ may be obtained by the conventional formulations based on the Floquet theorem for each ξ. The inverse transform (4) gives an expression of the scattered field $\psi^{(s)}(x, y)$ as

$$\begin{aligned}
\psi^{(s)}(x, y) &= \frac{d}{2\pi} \int_{-\pi/d}^{\pi/d} \overline{\psi}^{(s)}(x; \xi, y)\, d\xi \\
&= \frac{d}{2\pi} \int_{-\pi/d}^{\pi/d} \boldsymbol{f}_s^{(+)}(x; \xi, y)^t\, \overline{\boldsymbol{a}}_s^{(+)}(\xi, +0)\, d\xi. \tag{20}
\end{aligned}$$

An Expression of the far-zone field is obtained by using the cylindrical coordinate (ρ, ϕ) and applying the saddle-point method [8]. The integral in Eq. (20) is approximated for $\rho \to \infty$ as the following form:

$$\psi^{(s)}(\rho, \phi) \approx \frac{e^{i\,k_s\,\rho}}{\sqrt{k_s\,\rho}}\, p(\phi) \tag{21}$$

where the scattering pattern function $p(\phi)$ is given by

$$p(\phi) = \frac{k_s\, d\, \sin\phi}{\sqrt{i\,2\pi}}\, \overline{a}_{s,u}^{(+)}(\alpha_{-u}(k_s\,\cos\phi), +0). \tag{22}$$

In this expression, u is the closest integer number of $(d/\lambda_s)\cos\phi$ where λ_s denotes the wavelength in the surrounding media.

3. APPLICATION EXAMPLE I: PERIODIC ARRAY OF CIRCULAR CYLINDERS

3.1. Computational Details

In this section, we shall investigate a scattering problem on a infinitely periodic array of cylindrical objects situated parallel to each other as shown in Fig. 1. The cylindrical objects are identical and infinitely long in the z-direction, and consist of a homogeneous and isotropic material with the permittivity ε_c, the permeability μ_c, and the radius a. One of the cylinders is located at the origin and the cylinders are periodically spaced with a common distance d $(d > 2\,a)$ in the x-direction. The surrounding region is filled with a lossless, homogeneous, and isotropic material described by the permittivity ε_s and the permeability μ_s, and then the wavenumber in the surrounding media is written as $k_s = \omega\sqrt{\varepsilon_s\,\mu_s}$. In the previous section, we consider the scattering from a periodic structure contained in the half space $y \leq 0$, and show some relations between the incident and the scattered fields in the other half space $y > 0$. But, on this problem, the scatterers are contains in a layer $-a \leq y \leq a$, and the fields in the lower region $y < -a$ are also considerable.

The computation of electromagnetic scattering from two or more cylindrical objects has been efficiently performed with the recursive T-matrix algorithm (RTMA) [9]. Here we use a calculation technique of RTMA developed by Roussel [10] and Yasumoto *et al.* [11–14] to derive the T-matrices of periodic cylinder array for plane wave incidence. Following these methods, the scattering relation of the wave amplitudes
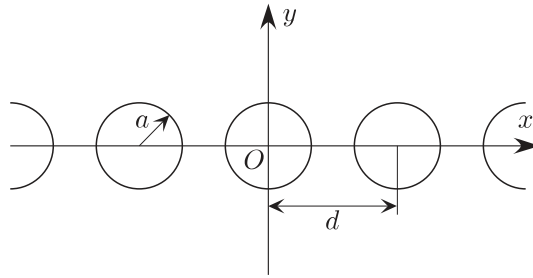

Figure 1. Geometry of a periodic array of circular cylinders.

is calculated in the following form

$$\begin{pmatrix} \overline{\boldsymbol{a}}_s^{(+)}(\xi, +0) \\ \overline{\boldsymbol{a}}_s^{(-)}(\xi, -0) \end{pmatrix} = \begin{pmatrix} \boldsymbol{S}_{11}(\xi) & \boldsymbol{S}_{12}(\xi) \\ \boldsymbol{S}_{21}(\xi) & \boldsymbol{S}_{22}(\xi) \end{pmatrix} \begin{pmatrix} \overline{\boldsymbol{a}}_s^{(-)}(\xi, +0) \\ \overline{\boldsymbol{a}}_s^{(+)}(\xi, -0) \end{pmatrix} \qquad (23)$$

$$\boldsymbol{S}_{11}(\xi) = \boldsymbol{Q}_s^{(+)}(\xi) \left(\boldsymbol{T}^{-1} - \boldsymbol{L}(k_s\,d, \xi\,d) \right)^{-1} \boldsymbol{P}_s^{(-)}(\xi) \qquad (24)$$

$$\boldsymbol{S}_{12}(\xi) = \boldsymbol{I} + \boldsymbol{Q}_s^{(+)}(\xi) \left(\boldsymbol{T}^{-1} - \boldsymbol{L}(k_s\,d, \xi\,d) \right)^{-1} \boldsymbol{P}_s^{(+)}(\xi) \qquad (25)$$

$$\boldsymbol{S}_{21}(\xi) = \boldsymbol{I} + \boldsymbol{Q}_s^{(-)}(\xi) \left(\boldsymbol{T}^{-1} - \boldsymbol{L}(k_s\,d, \xi\,d) \right)^{-1} \boldsymbol{P}_s^{(-)}(\xi) \qquad (26)$$

$$\boldsymbol{S}_{22}(\xi) = \boldsymbol{Q}_s^{(-)}(\xi) \left(\boldsymbol{T}^{-1} - \boldsymbol{L}(k_s\,d, \xi\,d) \right)^{-1} \boldsymbol{P}_s^{(+)}(\xi) \qquad (27)$$

where the (n, m)th-entries of the square matrices $\boldsymbol{Q}_s^{(\pm)}(\xi)$, $\boldsymbol{L}(\zeta, \eta)$, and $\boldsymbol{G}^{(\pm)}(\eta)$ are given as follows:

$$\left(\boldsymbol{Q}_s^{(\pm)}(\xi) \right)_{n,m} = \begin{cases} \frac{2}{d\,\beta_{s,n}(\xi)} \left(\frac{-i\,\alpha_n(\xi) \pm \beta_{s,n}(\xi)}{k_s} \right)^m & \text{for } m \geq 0 \\ \frac{2}{d\,\beta_{s,n}(\xi)} \left(\frac{i\,\alpha_n(\xi) \pm \beta_{s,n}(\xi)}{k_s} \right)^{-m} & \text{for } m < 0 \end{cases} \qquad (28)$$

$$\left(\boldsymbol{L}(\zeta, \eta) \right)_{n,m} = \sum_{l=1}^{\infty} H_{n-m}^{(1)}(l\,\zeta) \left[e^{i l \eta} + (-1)^{n-m}\, e^{-i l \eta} \right] \qquad (29)$$

$$\left(\boldsymbol{P}_s^{(\pm)}(\xi) \right)_{n,m} = \left(\frac{i\,\alpha_m(\xi) \pm \beta_{s,m}(\xi)}{k_s} \right)^n . \qquad (30)$$

The entries of $\boldsymbol{L}(\zeta, \eta)$ are given by the lattice sums, which are known to converge very slowly. An efficient calculation of lattice sums has been developed by Yasumoto and Yoshitomi [11], and we use it for practical computation. Also, the square diagonal matrix $\boldsymbol{T}$ is the T-matrix of the unit cylinder in isolation. Concrete representation of the T-matrix depends on the polarization, and the (n, m)th-entries are given by

$$(\boldsymbol{T})_{n,m} = \delta_{n,m} \frac{\sqrt{\varepsilon_c\mu_s}\, J_n(k_s a) J_n'(k_c a) - \sqrt{\varepsilon_s\mu_c}\, J_n'(k_s a) J_n(k_c a)}{\sqrt{\varepsilon_s\mu_c}\, H_n^{(1)'}(k_s a) J_n(k_c a) - \sqrt{\varepsilon_c\mu_s}\, H_n^{(1)}(k_s a) J_n'(k_c a)} \qquad (31)$$

for the TE polarization, and

$$(\boldsymbol{T})_{n,m} = \delta_{n,m} \frac{\sqrt{\varepsilon_s\mu_c}\, J_n(k_s\,a) J_n'(k_c a) - \sqrt{\varepsilon_c\mu_s}\, J_n'(k_s a) J_n(k_c a)}{\sqrt{\varepsilon_c\mu_s}\, H_n^{(1)'}(k_s a) J_n(k_c a) - \sqrt{\varepsilon_s\mu_c}\, H_n^{(1)}(k_s a) J_n'(k_c a)} \qquad (32)$$

for the TM polarization, where $k_c = \omega\,\sqrt{\varepsilon_c\,\mu_c}$ denotes the wavenumber inside the cylinder and $\delta_{n,m}$ denotes Kronecker's delta.

3.2. Line Source Excitation

First, we consider a line source excitation that gives the calculation of the Green function. The line source under consideration is situated parallel to the z-axis at $(x, y) = (x_0, y_0)$ where $y_0 > a$ or $y_0 < -a$. Then, the incident field is expressed as

$$\psi^{(i)}(x, y) = H_0^{(1)}(k_s \, \rho(x - x_0, y - y_0)) \tag{33}$$

where $\rho(x, y)$ is given as

$$\rho(x, y) = \sqrt{x^2 + y^2}. \tag{34}$$

The Hankel function of the first kind of order zero can be expressed by the Fourier integral representation [9]:

$$H_0^{(1)}(k_s \, \rho(x, y)) = \frac{1}{\pi} \int_{-\infty}^{\infty} \frac{1}{\sqrt{k_s^2 - \eta^2}} \, e^{i\left(\eta \, x + \sqrt{k_s^2 - \eta^2}|y|\right)} \, d\eta. \tag{35}$$

Using this relation, the amplitudes of the transformed incident field is obtained as follows:

$$\overline{a}_{s,n}^{(-)}(\xi, +0) = \begin{cases} \dfrac{2}{d \, \beta_{s,n}(\xi)} \, e^{-i(\alpha_n(\xi) \, x_0 - \beta_{s,n}(\xi) \, y_0)} & \text{for } y_0 > a \\ 0 & \text{for } y_0 < -a \end{cases} \tag{36}$$

$$\overline{a}_{s,n}^{(+)}(\xi, -0) = \begin{cases} 0 & \text{for } y_0 > a \\ \dfrac{2}{d \, \beta_{s,n}(\xi)} \, e^{-i(\alpha_n(\xi) \, x_0 + \beta_{s,n}(\xi) \, y_0)} & \text{for } y_0 < -a \end{cases} \tag{37}$$

for any integer n.

Here we consider a specific example of a periodic cylinder array with the following parameters: $\varepsilon_s = \varepsilon_0$, $\varepsilon_c = 4\,\varepsilon_0$, $\mu_s = \mu_c = \mu_0$, $d = 0.8\,\lambda_0$, $a = 0.4\,d$, and the line source is located at $(x_0, y_0) = (0, 2d)$. The same calculation with Eq. (20) yields the expression of the total field outside the periodic layer in the following form:

$$\psi(x, y) = \begin{cases} \psi^{(i)}(x, y) + \dfrac{d}{2\pi} \displaystyle\int_{-\pi/d}^{\pi/d} \boldsymbol{f}_s^{(+)}(x; \xi_l, y)^t \overline{\boldsymbol{a}}_s^{(+)}(\xi_l, +0) d\xi & \text{for } y > a \\ \dfrac{d}{2\,\pi} \displaystyle\int_{-\pi/d}^{\pi/d} \boldsymbol{f}_s^{(-)}(x; \xi_l, y)^t \, \overline{\boldsymbol{a}}_s^{(-)}(\xi_l, -0) \, d\xi & \text{for } y < -a \end{cases}. \tag{38}$$

The near-zone field can be computed by applying an appropriate numerical integration scheme. Let $\{\xi_l\}_{l=1}^{L}$ $(-\pi/d < \xi_1 < \xi_2 <$

$\cdots < \xi_L \leq \pi/d$), and $\{w_l\}_{l=1}^{L}$ be the sample points and the weights chosen by the numerical integration scheme. Then the scattered field is approximately expressed as

$$\psi(x,y) = \begin{cases} \psi^{(i)}(x,y) + \dfrac{d}{2\pi} \sum_{l=1}^{L} w_l \boldsymbol{f}_s^{(+)}(x;\xi_l,y)^t \overline{\boldsymbol{a}}_s^{(+)}(\xi_l,+0) & \text{for } y > a \\[2em] \dfrac{d}{2\pi} \sum_{l=1}^{L} w_l \, \boldsymbol{f}_s^{(-)}(x;\xi_l,y)^t \, \overline{\boldsymbol{a}}_s^{(-)}(\xi_l,-0) & \text{for } y < -a \end{cases}.$$

(39)

We choose that the truncation order is $N = 10$ and the location of observation point is $(x,y) = (0, -d)$. Figure 2 shows the intensity of the total field at the observation point as function of the number of integration segments L. The dotted and the dashed curves are the results of the trapezoidal and the Gauss-Legendre methods, respectively, and they converge slowly. To consider the origin of slow convergence, the transformed field, which is the integrand to calculate the total field, is plotted as function of the normalized transform parameter $\xi \, d/(2\,\pi)$ in Fig. 3. As written in Eq. (3), the transformed functions has a periodic property in terms of the transform parameter ξ with the period $2\,\pi/d$ and the horizontal range of Fig. 3 gives a periodicity cell. The trapezoidal method is known to usually provide accurate results to integrate smooth periodic functions over one period. However, Fig. 3 shows that the curves of the integrand are not smooth at $\xi \, d/(2\,\pi) = \pm 0.2$. These points are given by the Wood-Rayleigh anomalies that are known to occur when diffracted field of a spectral order propagates along the grating surface and cause abrupt changes in the power diffracted into the other orders. Then the x-directional propagation constant ξ has to satisfy $\alpha_n(\xi) = \pm k_s$ at the anomalies and, in the present formulation, the anomalies are degenerated to two points

$$\xi = \pm k_s - v \, \frac{2\,\pi}{d} \tag{40}$$

where v is the closest integer number of $\pm d/\lambda_s$. It is well known, if there are discontinuities or singularities of the integrand or of its derivative and we know where they are, the integration range should be split at these points and analyze each subinterval. Here we split the integration interval at the Wood-Rayleigh anomalies and apply the Gauss-Legendre method for each subinterval. The integration interval is divided into two subinterval by considering the periodicity and the sample point number L is divided in the ratio of the subinterval widths.

The solid curves in Fig. 2 are the results and show much improvement of convergence. We do not know the exact values of the field intensity, and the most reliable values in Fig. 2, which are given by solid curves with $N = 10$ and $L = 100$, are used as the references to estimate the errors in the following. When the Gauss-Legendre method is used for the split subinterval, the results show that 0.1% accuracy is achieved
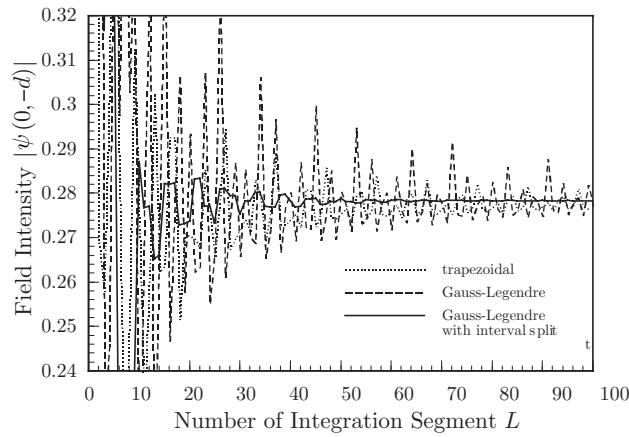
(a) TE polarization
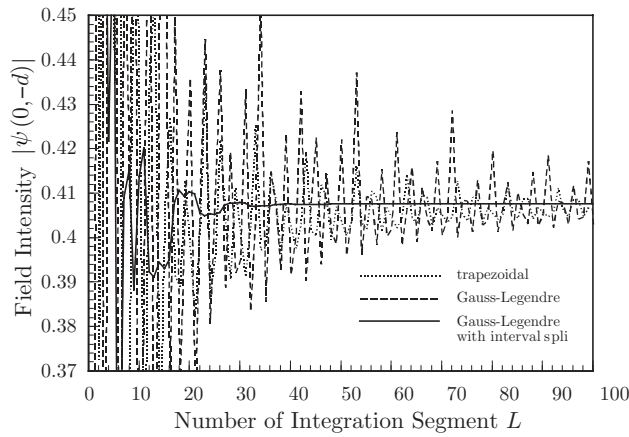
(b) TM polarization

Figure 2. Calculated intensity of the total field at $(x, y) = (0, -d)$ for a line source excitation as function of the number of integration segments L.

with $L = 60$ for TE polarization (the referred value is 0.2783) and $L = 37$ for TM polarization (the referred value is 0.40763). Also, the convergence with respect to the truncation order N is shown in Fig. 4. The numerical results are computed by the Gauss-Legendre method for the splitted subinterval with the same parameters as for
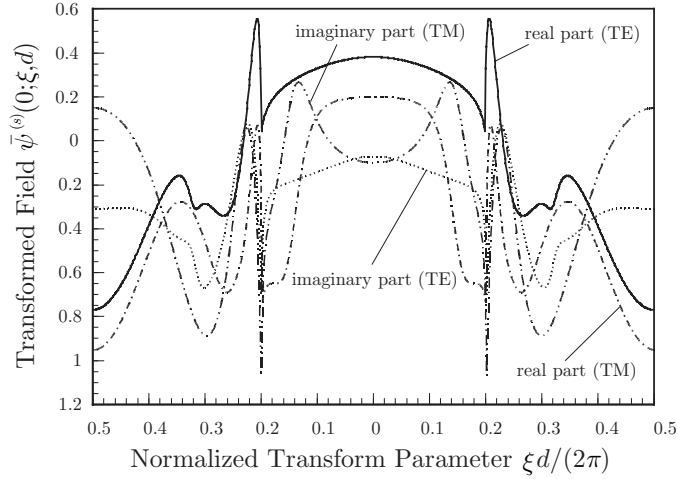
Figure 3. Transformed field at $(x, y) = (0, -d)$ for a line source excitation as function of the normalized transform parameter.
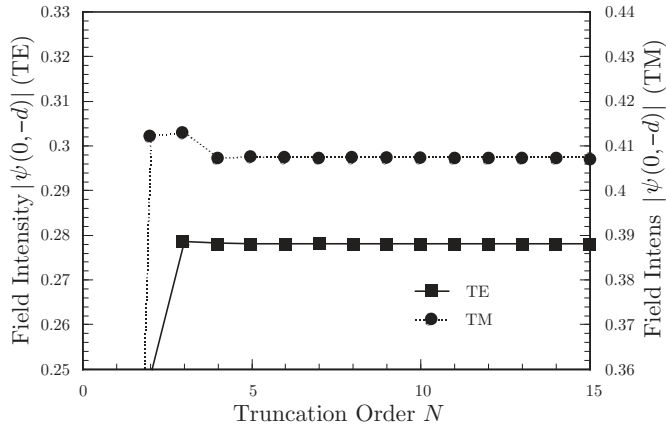
Figure 4. Calculated intensity of the total field at $(x, y) = (0, -d)$ for a line source excitation as function of the truncation order N.

Fig. 2, but we use the integration segment number of $L = 70$. It is observed that 0.1% accuracy is achieved with only $N = 4$ for both TE and TM polarizations. The total field intensities outside the periodic array layer are calculated with $N = 5$ and $L = 70$ by changing the observation point, and shown in Fig. 5. The positions of cylinders are indicated by the white dashed lines. Also, Fig. 6 shows the absolute values of the scattering pattern function $p(\phi)$ calculated by Eq. (22) with $N = 5$. As shown in Sec. 2.3, the far-zone fields can be calculated without use of the numerical integration.

We examine the reciprocal property to validate the formulation. Let $\psi_{pq}(x_p, y_p; x_q, y_q)$ be the field observed at (x_p, y_p) for a line source located at (x_q, y_q). Then we define the reciprocity error by

$$\sigma(x_p, y_p; x_q, y_q) = \psi_{pq}(x_p, y_p; x_q, y_q) - \psi_{qp}(x_q, y_q; x_p, y_p). \qquad (41)$$

The reciprocity theorem requires that this function should be zero when both (x_p, y_p) and (x_q, y_q) are located outside the periodic array layer. We fix one point $(x_q, y_q) = (0, 2d)$ and the other point (x_p, y_p) is moved on lines $y = \pm d$. Figure 7 shows the calculated values of $|\sigma(x, \pm d; 0, 2d)|$ that are computed in the standard double-precision arithmetic. The largest value is about 1.2×10^{-15} that is in the order of round-off error, and the reciprocal property is completely satisfied in the sense of numerical analysis. Also, the results of the present formulation are compared with those of the conventional RTMA [9] for the scattering from a finite number of cylinders. When the number of cylinder is denoted by M, the conventional RTMA requires the inversion of $M(2N+1) \times M(2N+1)$ matrix though the present formulation deals with $(2N+1) \times (2N+1)$ matrices only. From the physical point of view, if the number of cylinders is large enough, one can expect that the fields near the line source are not noticeably different in both methods. Here we consider 81 cylinders located at $(x, y) = (m\,d, 0)$ for $m = 0, \pm 1, \ldots, \pm 40$, and the intensity of the total field at $(x, y) = (0, -d)$ is calculated by the conventional RTMA. The obtained values are 0.2783 for TE polarization and 0.4076 for TM polarization, which are in very good agreement with the results of the present formulation.

3.3. Hermite-Gaussian Beam Incidence

Next, we consider a two-dimensional Hermite-Gaussian beam incidence. The commonly used expression of the Hermite-Gaussian beam is derived by using a para-axial approximation and does not satisfy the Helmholtz equation (8). Hence, we use the expression in terms of a superposition of a finite number of complex source
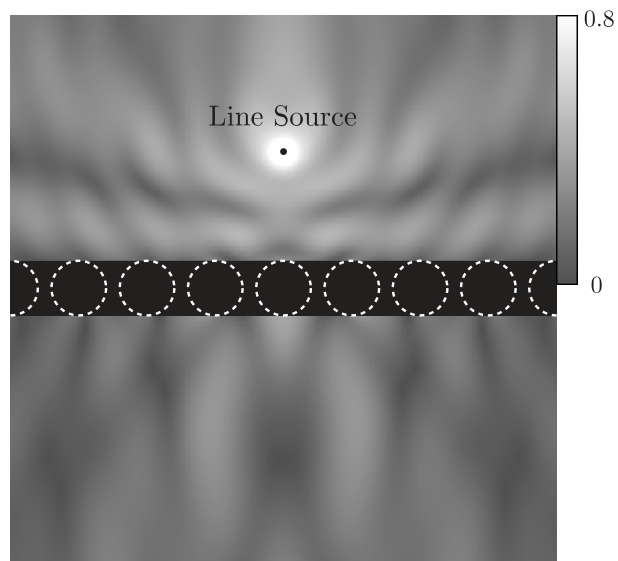
(a) TE polarization
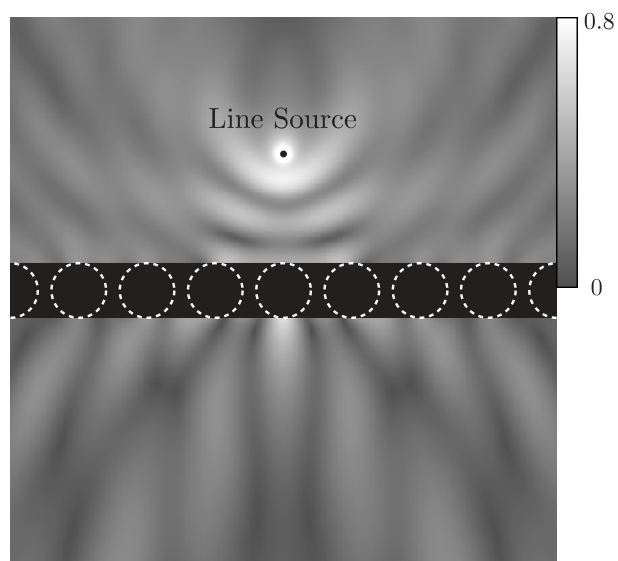
(b) TM polarization

Figure 5. Distribution of the total field intensity outside the periodic array layer for a line source located at $(x_0, y_0) = (0, 2d)$.
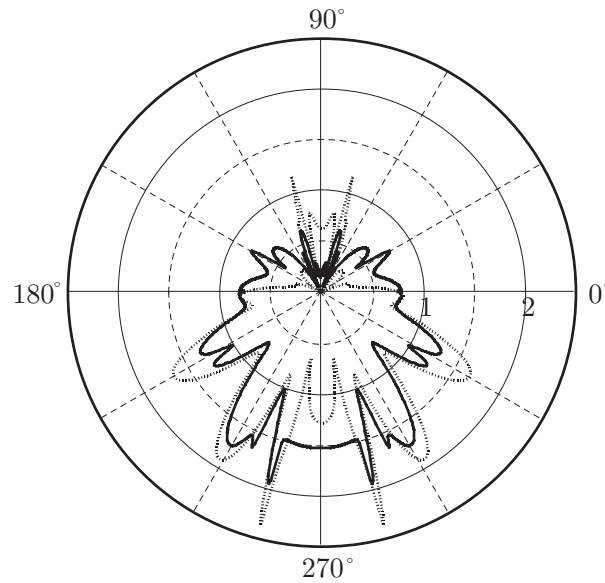
Figure 6. Scattering pattern of a periodic cylinder array for a line source located at $(x_0, y_0) = (0, 2d)$. The solid and the dotted curves denote the results for the TE and the TM polarizations, respectively.
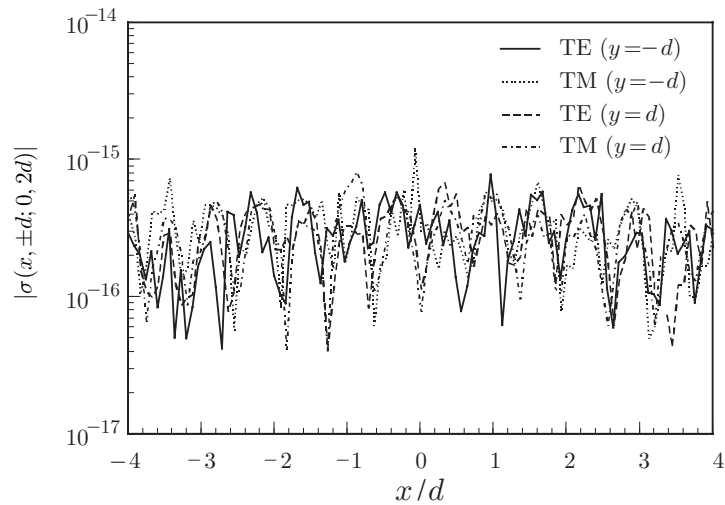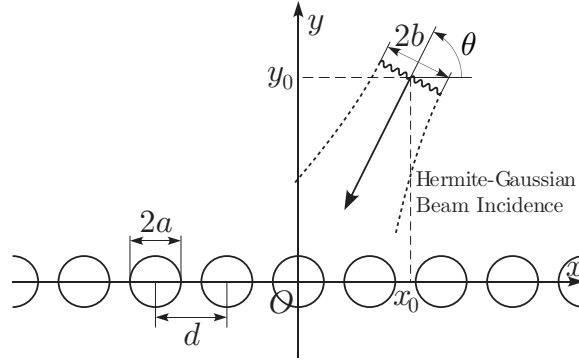

Figure 7. Calculated values of the reciprocity errors.

Figure 8. Geometry of the Hermite-Gaussian beam illuminating a periodic cylinder array.

point multipole fields [15], which satisfies the Helmholtz equation (8). The lth-order Hermite-Gaussian beam under consideration propagates along a direction perpendicular to the z-axis and the fields are uniform in the z-direction. The beam waist is located at $(x, y) = (x_0, y_0)$, and we denote the spot size at the beam waist by w_0 and the propagation angle by θ (Fig. 8). We write $b = k_s \, w_0{}^2/2$, and consider the radiated fields from a complex source point $(x_0', y_0') = (x_0 - i \, b \cos\theta, y_0 - i \, b \sin\theta)$. The beam expression is given by

$$\psi^{(i)}(x, y) = (-1)^l \, k_s \, \sqrt[4]{\frac{\pi}{2}} \, \sqrt{\frac{l! \, w_0}{2}} \, e^{-k_s \, b}$$
$$\times \sum_{m=0}^{[l/2]} \frac{2^{-m} \, w_0{}^{l-2\,m}}{m! \, (l - 2\,m)!} \, g^{(l-2m)}(x - x_0', y - y_0') \qquad (42)$$

with

$$g^{(m)}(x, y) = \left(-\sin\theta \, \frac{\partial}{\partial x} + \cos\theta \, \frac{\partial}{\partial y} \right)^m H_0^{(1)}(k_s \, \rho(x, y)) \qquad (43)$$

where $[l/2]$ is $l/2$ or $(l - 1)/2$ depending on whether l is even or odd, respectively. The complex distance $\rho(x, y)$ is defined by Eq. (34) where the branch is chosen so as that its real part is not negative. The wavy line in Fig. 8 is the branch cut. Here the beam is supposed to illuminate the periodic array from the upper side ($y_0 > a + b \, |\cos\theta|$ and $0 < \theta < \pi$). The Hankel function of the first kind of order zero is also expressed by Eq. (35). Then the multipole field $g^{(m)}(x, y)$ for

$y < 0$ can be rewritten as

$$g^{(m)}(x,y) = \frac{(-i)^m}{\pi} \int_{-\infty}^{\infty} \frac{\left(\eta \sin\theta + \sqrt{k_s^2 - \eta^2} \cos\theta \right)^m}{\sqrt{k_s^2 - \eta^2}} \, e^{i\left(\eta x - \sqrt{k_s^2 - \eta^2} y \right)} \, d\eta,$$

(44)

and the Rayleigh coefficients of the transformed incident field are derived as follows:

$$\overline{a}_{s,n}^{(-)}(\xi, +0) = \frac{i^l \, k_s \, \sqrt[4]{2\,\pi} \, \sqrt{l! \, w_0}}{d \, \beta_{s,n}(\xi)} \, e^{-k_s \, b - i\left(\alpha_n(\xi) \, x_0' - \beta_{s,n}(\xi) \, y_0' \right)}$$

$$\times \sum_{m=0}^{[l/2]} \frac{(-2)^{-m} \left[w_0 \left(\alpha_n(\xi) \, \sin\theta + \beta_{s,n}(\xi) \, \cos\theta \right) \right]^{l-2m}}{m! \, (l - 2\,m)!}$$

(45)

$$\overline{a}_{s,n}^{(+)}(\xi, -0) = 0.$$

(46)

We show numerical results of the second-order Hermite-Gaussian beam illuminating the same array of circular cylinders as in the previous subsection. The parameters for the incident beam are chosen as follows: $(x_0, y_0) = (3\,d, 3\sqrt{3}\,d)$, $w_0 = 1.5\,\lambda_0$, and $\theta = 60°$. Figure 9 gives the ξ-dependence of the transformed field at an observation point
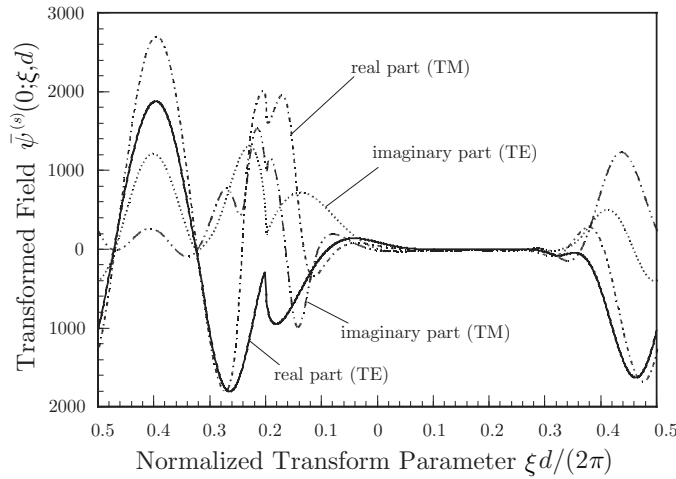
Figure 9. Transformed field at $(x, y) = (0, -d)$ for the second-order Hermite-Gaussian beam incidence as function of the normalized transform parameter $\xi \, d/(2\,\pi)$.
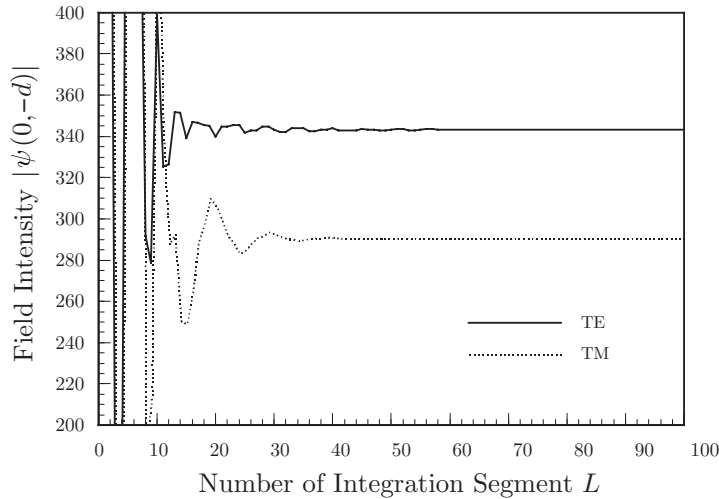
Figure 10. Calculated intensity of the total field at $(x, y) = (0, -d)$ for the second-order Hermite-Gaussian beam incidence as function of the number of integration segments L.

$(x, y) = (0, -d)$, computed with the truncation order $N = 10$. The spectrum of beam field is concentrated on a narrow band and then the values are small for $0 < \xi\, d/(2\,\pi) < 0.3$. The Wood-Rayleigh anomalies are found at $\xi\, d/(2\,\pi) = \pm 0.2$ (the non-smooth point for $\xi\, d/(2\,\pi) = 0.2$ can be observed by enlarging the scale), and the integration interval for the inverse transform should be split at these points. We apply the Gauss-Legendre method for each subintervals as same as in the previous subsection and Fig. 10 shows the calculated intensity of the total field at $(x, y) = (0, -d)$ as function of the number of integration segments L. The results show that $0.1\,\%$ accuracy is achieved with $L = 46$ for TE polarization (the referred value is 343.22) and $L = 40$ for TM polarization (the referred value is 290.837). The total field intensities outside the periodic array layer are computed with $N = 5$ and $L = 60$, and shown in Fig. 11. Also, the scattering patterns computed with $N = 5$ are shown in Fig. 12. The second-order Hermite-Gaussian beam consists of three beam lobes, and we can observe the transmitted and the reflected beams in the 0th- and the -1st-order of diffraction.
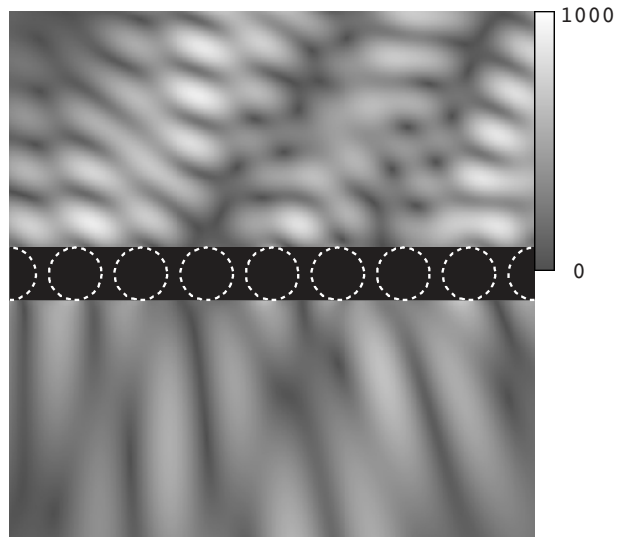
(a) TE polarization
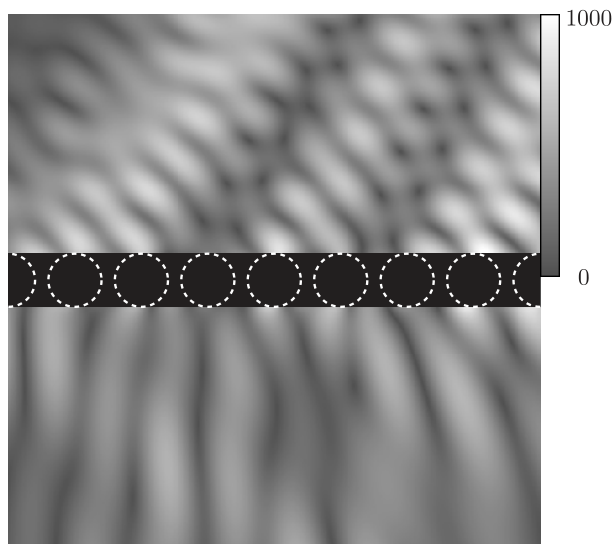
(b) TM polarization

Figure 11. Distribution of the total field intensity outside the periodic array layer for the second-order Hermite-Gaussian beam incidence.
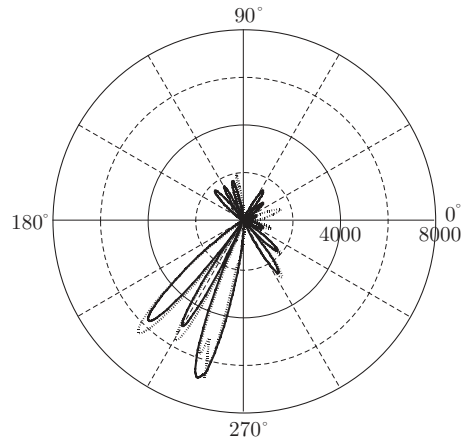
Figure 12. Scattering pattern of a periodic cylinder array for the second-order Hermite-Gaussian beam incidence. The solid and the dotted curves denote the results for the TE and the TM polarizations, respectively.

4. APPLICATION EXAMPLE II: LAMELLAR GRATING

4.1. Computational Details

For the second example of periodic structures, a lamellar grating schematically shown in Fig. 13 is considered in this section. The grating grooves are ruled on a linear isotropic substrate described by the permittivity ε_c and the permeability μ_c, and parallel to the z-axis. The direction of periodicity is parallel to the x-axis, and we denote the grating period by d, the grating depth by h, and the groove width by g. The cover region is filled with a lossless, homogeneous, and isotropic material described by the permittivity ε_s and the permeability μ_s. The incident field is supposed to propagate downward in the cover region.

All the components of the transformed electromagnetic fields for each ξ are pseudo-periodic functions of x, and thus the scattering-matrix can be obtained by the rigorous coupled-wave method (RCWM) [16, 17]. This method expands the pseudo-periodic field components in the generalized Fourier series, and the Maxwell equations yield a coupled differential-equation set for the Fourier coefficients of field components. For the lamellar gratings, the coefficient matrix of the coupled differential-equation set is constant in the groove region, and the general solution is obtained by solving an eigenvalue problem. The electromagnetic fields outside the groove region are also expressed
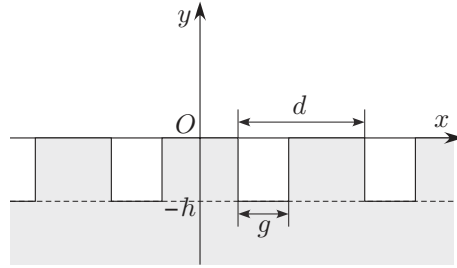
Figure 13. Geometry of a lamellar grating.

by the Rayleigh expansions. The solution obtained inside the groove region is matched to the Rayleigh expansions at the top and the bottom of the grooves and the scattering-matrix can be calculated. Many formulations of the method have been proposed by many researchers. Our formulation used to derive the scattering-matrix for each ξ is described in Ref. [18].

4.2. Metallic Grating with Line Source Excitation

This subsection provides numerical results of a specific example of metallic grating for a line source excitation. The grating parameters are chosen as follows: $d = 0.6\,\lambda_0$, $g = 0.4\,d$, $h = 0.5\,\lambda_0$, $\varepsilon_c = (1.3 + i\,7.6)^2\,\varepsilon_0$, $\varepsilon_s = \varepsilon_0$, and $\mu_c = \mu_s = \mu_0$. The line source is parallel to the z-axis and located at $(x_0, y_0) = (0, 2\,d)$. The transformed scattered field at an observation point $(x, y) = (0, d)$ are calculated with the truncation order $N = 25$, and plotted as functions of the normalized transform parameter $\xi\,d/(2\,\pi)$ in Fig. 14. The Wood-Rayleigh anomalies are found at $\xi\,d/(2\,\pi) = \pm 0.4$ and, to apply numerical integration, the integration interval for the inverse transform should be split at these points. Figure 15 shows the calculated results of the field intensity at the observation point as function of the number of integration segments L. The solid curves are the results of the Gauss-Legendre method, and show slow convergence. The reason of slow convergence is thought to be the strong singularity at the anomalies, and the double exponential method given by the dotted curves provides better convergence. The most reliable values calculated with $N = 25$ and $L = 200$ are used as the reference values (0.543195 for TE polarization and 0.48585 for TM polarization). The results of the double exponential method show that 0.1 % accuracy is achieved with $L = 63$ for TE polarization and $L = 58$ for TM polarization. The convergence with respect to the truncation order N is shown in

Fig. 16. It is well known that RCWM for TM polarization and metallic
gratings requires large truncation order, and the results show that $0.1\,\%$
accuracy is achieved with $N = 7$ for TE polarization and $N = 17$ for
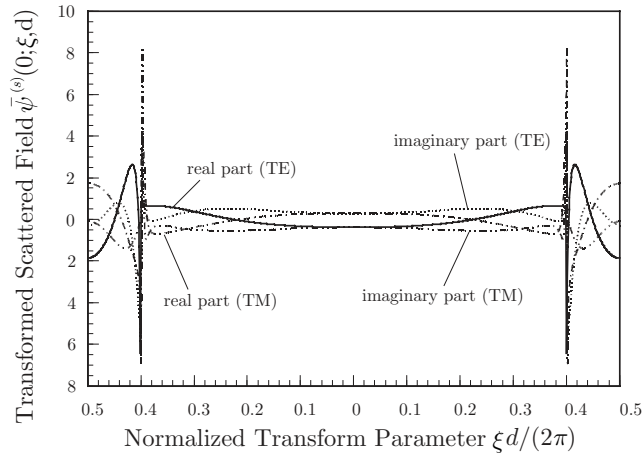

Figure 14. Transformed scattered field at $(x, y) = (0, d)$ for a line
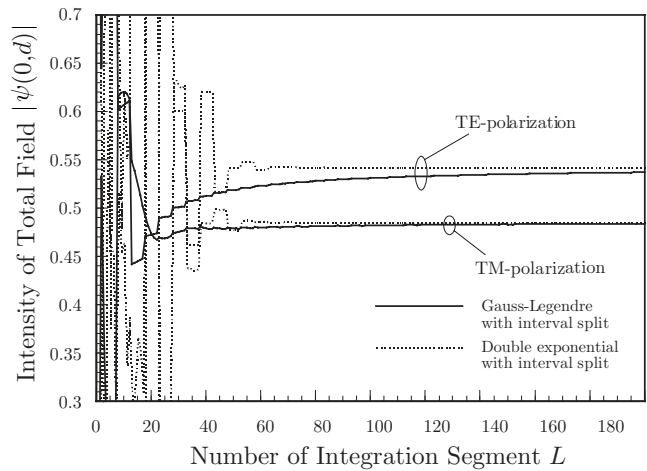source excitation as function of the normalized transform parameter.

Figure 15. Calculated intensity of the total field at $(x, y) = (0, d)$
for a line source excitation as function of the number of integration
segments L.
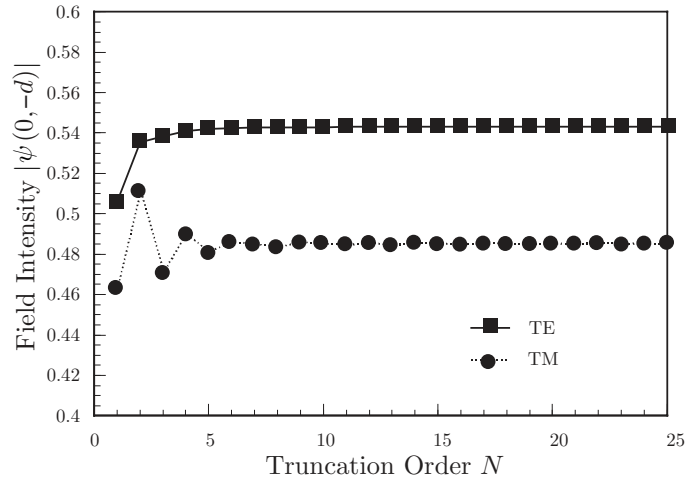
Figure 16. Calculated intensity of the total field at $(x, y) = (0, d)$ for a line source excitation as function of the truncation order N.
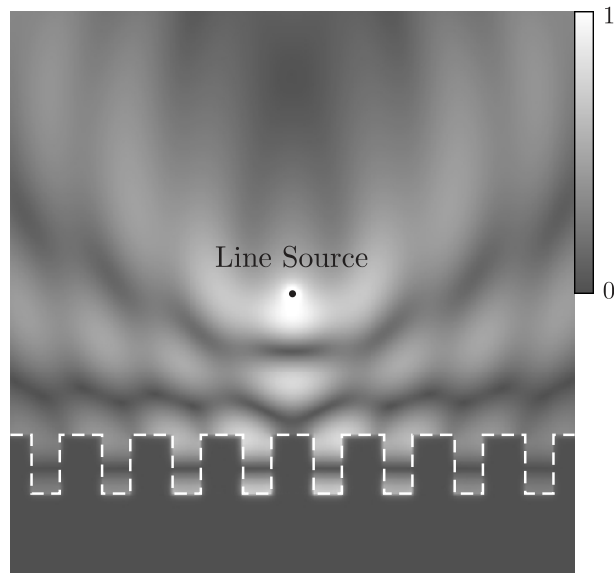
TM polarization. The field intensity near the grating is calculated with $N = 20$ and $L = 80$ by changing the observation point, and plotted in Fig. 17. The position of grating surface is indicated by the white dashed line. Since the substrate is assumed to be a conducting material, the fields decay rapidly inside the substrate. The field for TE polarization does not propagate into the grooves because of the cutoff. As the result, the field distribution for TE polarization seems to be similar to that near the metallic plate. On the other hand, the field distribution for TM polarization shows strong effects of the grooves. Also, Fig. 18 shows the absolute values of the scattering pattern function $p(\phi)$ calculated with $N = 20$. The pattern shows abrupt changes in intensity at the anomalies, and the changes for TM polarization is much more noticeable than those for TE polarization.

4.3. Lossless Grating with Hermite-Gaussian Beam Incidence

For a lamellar grating made of a lossless material with a Hermite-Gaussian beam incidence, the transformed scattered field at an observation point is shown in Fig. 19. The grating parameters are chosen as follows: $d = 0.6\,\lambda_0$, $g = 0.4\,d$, $h = 0.5\,\lambda_0$, $\varepsilon_c = 1.5^2\,\varepsilon_0$, $\varepsilon_s = \varepsilon_0$, and $\mu_c = \mu_s = \mu_0$. The incident field is the first-order Hermite-Gaussian beam and the beam parameters are chosen
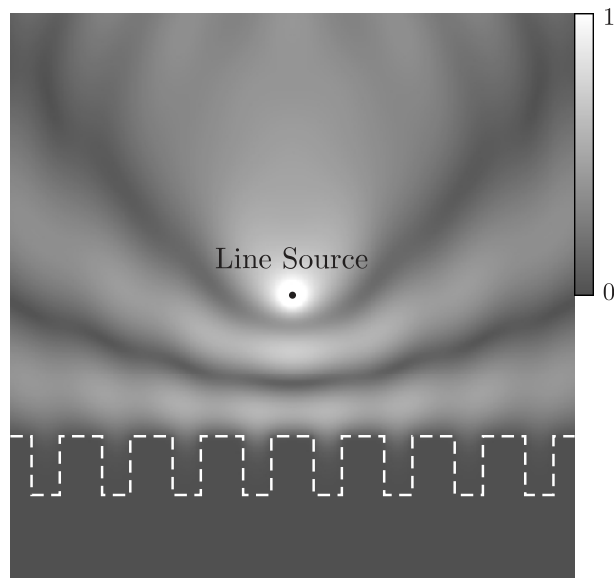
(a) TE polarization

(b) TM polarization

Figure 17. Field intensity near a lamellar grating with a line source excitation.
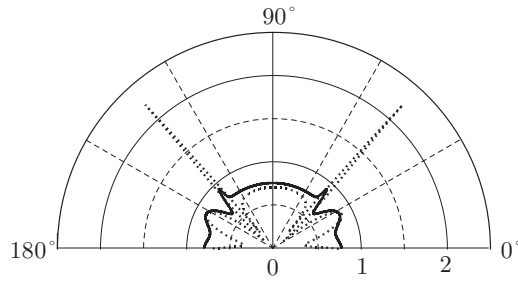
Figure 18. Scattering pattern of a lamellar grating for a line source excitation. The solid and the dotted curves denote the results for the TE and the TM polarizations, respectively.
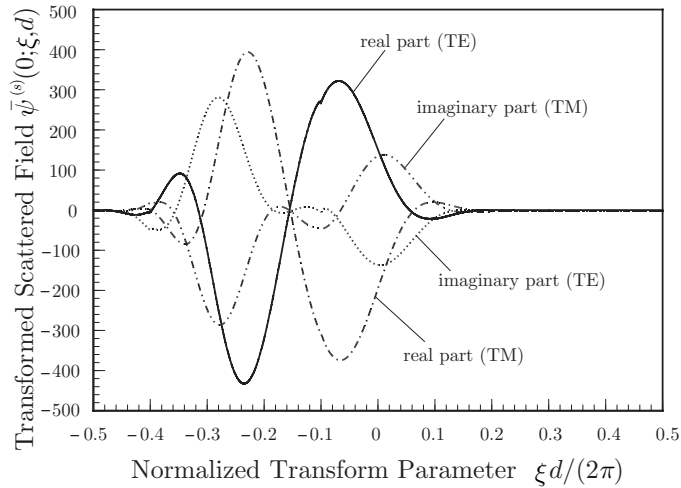

Figure 19. Transformed scattered field at $(x, y) = (0, d)$ for a first-order Hermite-Gaussian beam incidence as function of the normalized transform parameter.

as follows: $(x_0, y_0) = (2\,d, (4 + 2\sqrt{3})d)$, $w_0 = 1.5\,\lambda_0$, and $\theta = 75°$. The transformed scattered fields at $(x, y) = (0, d)$ are calculated with the truncation order $N = 15$.   The Wood-Rayleigh anomalies are not noticeable, but we can find them at the same positions $\xi\,d/(2\,\pi) = \pm 0.4$ (non-smooth points are clearly observed by enlarging the scale) because the dielectric constants in the cover region and the grating period are same with those in Fig. 14. In this example, there exist also the Wood-Rayleigh anomalies associated with the diffracted fields in the substrate
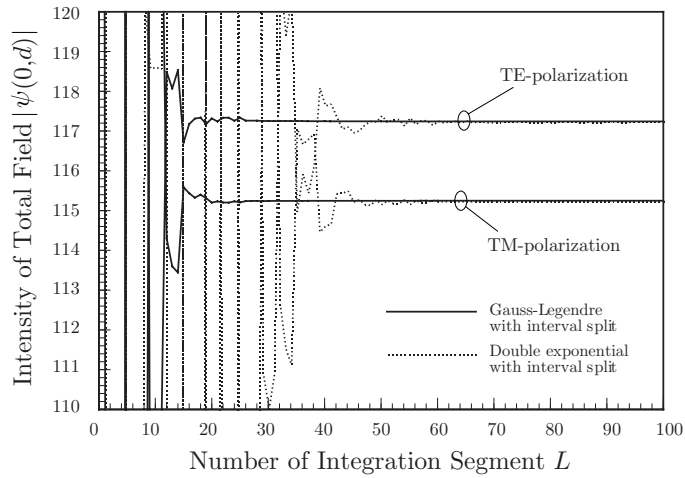
Figure 20. Calculated intensity of the total field at $(x, y) = (0, d)$ for a first-order Hermite-Gaussian beam incidence as function of the number of integration segments L.
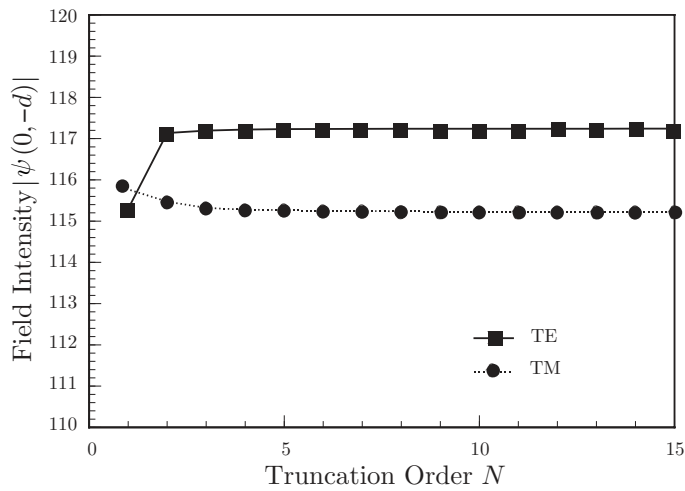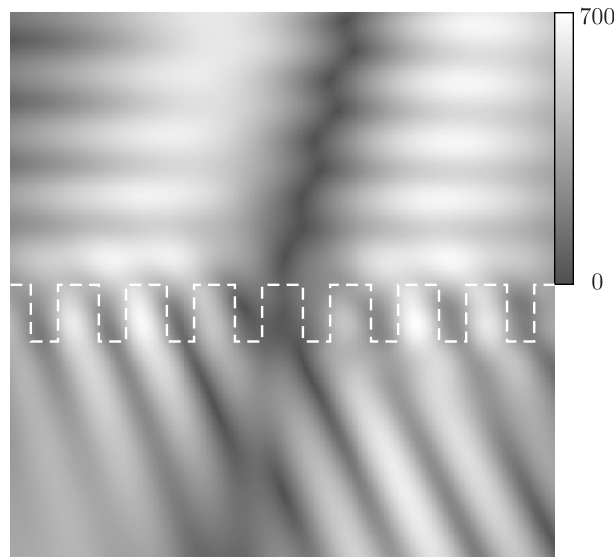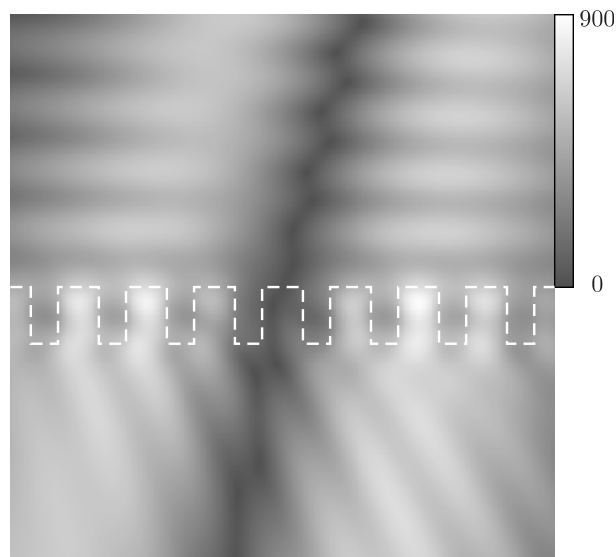

Figure 21. Calculated intensity of the total field at $(x, y) = (0, d)$ for a first-order Hermite-Gaussian beam incidence as function of the truncation order N.

(a) TE polarization

(b) TM polarization

Figure 22. Field intensity near a lamellar grating with a Hermite-Gaussian beam incidence.
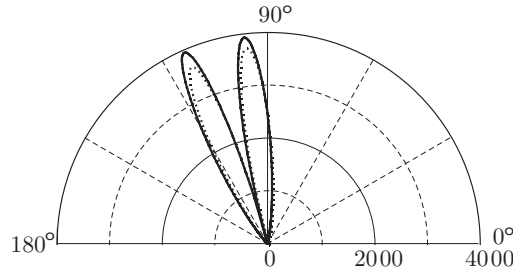
Figure 23. Scattering pattern of a lamellar grating for a Hermite-Gaussian beam incidence. The solid and the dotted curves denote the results for the TE and the TM polarizations, respectively.

region. Let λ_c and k_c be the wavelength and the wavenumber in the substrate region. Then the position of the anomalies are given by

$$\xi = \pm k_c - v\,\frac{2\,\pi}{d} \tag{47}$$

where v is the closest integer number of $\pm d/\lambda_c$, and we can find the anomalies at $\xi\,d/(2\,\pi) = \pm 0.1$ in Fig. 19. Of course, the Wood-Rayleigh anomalies associated with the substrate region are not noticeable when k_c is far from the real-axis, and this is the reason why we did not find them in the metallic grating shown in the previous subsection. Anyway, we split the integration interval for the inverse transform into four subintervals at the Wood-Rayleigh anomalies, and apply numerical integration schemes. Figure 20 shows the convergence of field intensity computed by the Gauss-Legendre and the double exponential methods with $N = 15$. As shown in Fig. 19, the singularity of the endpoints are not strong for each subinterval, and therefore the Gauss-Legendre method shows faster convergence. The most reliable values calculated with $N = 15$ and $L = 100$ are used as the reference values (117.24 for TE polarization and 115.25 for TM polarization), and the Gauss-Legendre method show that $0.1\,\%$ accuracy is achieved with $L = 16$ for TE polarization and $L = 19$ for TM polarization. Also, Fig. 21 provides the convergence with respect to the truncation order N, and the numerical results shows that $0.1\,\%$ accuracy is achieved with $N = 2$ for TE polarization and $N = 3$ for TM polarization. The field intensity near the grating is calculated with $N = 5$ and $L = 30$ and plotted in Fig. 22. Also the scattering pattern calculated with $N = 5$ is given by Fig. 23. The first-order Hermite-Gaussian beam consists of two beam lobes, and Fig. 23 shows that the scattering field in the cover region $y > 0$ is mainly composed by the reflection beam in the zeroth-order of

diffraction. Hence, the pattern stripes in the cover region are parallel to the grating surface.

5. CONCLUSION

This paper has proposed PPFT that is an idea to approach the electromagnetic scattering problems from the periodic structures with non-plane incident waves. PPFT makes arbitrary functions pseudo-periodic and the conventional approaches based on the Floquet theorem become applicable. We have shown numerical results of two periodic structures. The first is a periodic array of circular cylinders and RTMA is applied for the problems with a line source excitation and a Hermite-Gaussian beam incidence. The second example is a lamellar grating and RCWM is applied for scattering problems from a metallic grating with a line source excitation and from a lossless grating with a Hermite-Gaussian beam incidence. The numerical results of periodic cylinder array with line source excitation are validated by comparing with the scattering from an array of large number of cylinders and also shown that the reciprocal property for the line source excitation is completely satisfied in the sense of numerical analysis. The near field analysis requires a numerical integration with respect to the transform parameter over a finite interval. The integrand function is generally non-smooth at the Wood-Rayleigh anomalies, which are degenerated due to PPFT, and we should split the integration interval into several subintervals for numerical integration. Also, the convergence of numerical integration is shown to be depend on the endpoint singularity of each subinterval. In this paper, we dealt with periodic structures in which the surface wave cannot propagate along the periodic direction. However, the analyses for such structures may require a consideration of the Wood-resonance anomalies and are left for the future works.

REFERENCES

1. Petit, R. (ed.), *Electromagnetic Theory of Gratings*, Vol. 22 of Topics in Current Physics, Springer-Verlag, Berlin, 1980.
2. Kriezis, Em. E., P. K. Pandelakis, and A. G. Papagiannakis, "Diffraction of a Gaussian beam from a periodic planar screen," *J. Opt. Soc. Am. A*, Vol. 11, No. 2, 630–636, 1994.
3. Yang, J., L. W. Li, K. Yasumoto, and C. H. Liang, "Two-dimensional scattering of a Gaussian beam by a periodic array of circular cylinders," *IEEE Trans. Geosci. Remote Sensing*, Vol. 43, No. 2, 280–285, 2005.

4. Caloz, C., A. K. Skrivervik, and F. E. Gardiol, "An efficient method to determine Green's functions of a two-dimensional photonic crystal excited by a line source—the phased-array method," *IEEE Trans. Microwave Theory and Techniques*, Vol. 50, No. 5, 1380–1391, 2002.

5. Jandieri, V., H. Toyama, and K. Yasumoto, "Radiation from a localized line source in two-dimensional photonic crystals," *The Papers of Technical Meeting on Electromagnetic Theory, IEE Japan*, EMT-06-13, 2006.

6. Nakayama, J., "Periodic Fourier transform and its application to wave scattering from a finite periodic surface," *IEICE Trans. Electron.*, Vol. E83-C, No. 3, 481–487, 2000.

7. Watanabe, K. and K. Kuto, "Numerical analysis of optical waveguides based on periodic Fourier transform," *Progress In Electromagnetics Research*, PIER 64, 1–21, 2006.

8. Balanis, C. A., *Advanced Engineering Electromagnetics*, Wiley, New York, 1989.

9. Chew, W. C., *Waves and Fields in Inhomogeneous Media*, Van Nostrand Reinhold, New York, 1990.

10. Roussel, H., W. C. Chew, F. Jouvie, and W. Tabbara, "Electromagnetic scattering from dielectric and magnetic gratings of fibers — a T-matrix solution," *J. Electromagnetic Waves and Appl.*, Vol. 10, No. 1, 109–127, 1996.

11. Yasumoto, K. and K. Yoshitomi, "Efficient calculation of lattice sums for free-space periodic Green's function," *IEEE Trans. Antennas Propagat.*, Vol. 47, No. 6, 1050–1055, 1999.

12. Kushta, T. and K. Yasumoto, "Electromagnetic scattering form periodic array of two circular cylinders per unit cell," *Progress In Electromagnetics Research*, PIER 29, 69–85, 2000.

13. Toyama, H. and K. Yasumoto, "Eelectromagnetic scattering from periodic arrays of composite circular cylinder with internal cylindrical scatterers," *Progress In Electromagnetics Research*, PIER 52, 321–333, 2005.

14. Jia, H. and K. Yasumoto, "Rigorous analysis of guided modes of two-dimensional metallic electromagnetic crystal waveguides," *J. Electromagnetic Waves and Appl.*, Vol. 19, No. 14, 1919–1933, 2005.

15. Yokota, M., T. Takenaka, and O. Fukumitsu, "Scattering of a Hermite-Gaussian beam mode by parallel dielectric circular cylinders," *J. Opt. Soc. Am. A*, Vol. 3, No. 4, 580–586, 1986.

16. Knop, K., "Rigorous diffraction theory for transmission phase gratings with deep rectangular grooves," *J. Opt. Soc. Am.*, Vol. 68, No. 9, 1206–1210, 1978.

17. Moharam, M. G. and T. K. Gaylord, "Diffraction analysis of dielectric surface-relief gratings," *J. Opt. Soc. Am.*, Vol. 72, No. 10, 1385–1392, 1982.

18. Watanabe, K., J. Pištora, M. Foldyna, K. Postava, and J. Vlček, "Numerical study on the spectroscopic ellipsometry of lamellar gratings made of lossless dielectric materials," *J. Opt. Soc. Am. A*, Vol. 22, No. 4, 745–751, 2005.